Monthly Notices
of the
ROYAL ASTRONOMICAL SOCIETY

MNRAS **434,** 1889–1901 (2013) doi:10.1093/mnras/stt1081
Advance Access publication 2013 August 1

HESS and *Fermi*-LAT discovery of γ-rays from the blazar 1ES 1312−423

HESS Collaboration, A. Abramowski,[1] F. Acero,[2] F. Aharonian,[3,4,5] A. G. Akhperjanian,[6,5] E. Angüner,[7] G. Anton,[8] S. Balenderan,[9] A. Balzer,[10,11] A. Barnacka,[12] Y. Becherini,[13,14,15⋆] J. Becker Tjus,[16] K. Bernlöhr,[3,7] E. Birsin,[7] E. Bissaldi,[17] J. Biteau,[15⋆] C. Boisson,[18] J. Bolmont,[19] P. Bordas,[20] J. Brucker,[8] F. Brun,[3] P. Brun,[21] T. Bulik,[22] S. Carrigan,[3] S. Casanova,[23,3] M. Cerruti,[18,24] P. M. Chadwick,[9] R. Chalme-Calvet,[19] R. C. G. Chaves,[21,3] A. Cheesebrough,[9] M. Chrétien,[19] S. Colafrancesco,[25] G. Cologna,[13] J. Conrad,[26] C. Couturier,[19] M. Dalton,[27†] M. K. Daniel,[9] I. D. Davids,[28] B. Degrange,[15] C. Deil,[3] P. deWilt,[29] H. J. Dickinson,[26] A. Djannati-Ataï,[14] W. Domainko,[3] L.O'C. Drury,[4] G. Dubus,[30] K. Dutson,[31] J. Dyks,[12] M. Dyrda,[32] T. Edwards,[3] K. Egberts,[17] P. Eger,[3] P. Espigat,[14] C. Farnier,[26] S. Fegan,[15] F. Feinstein,[2] M. V. Fernandes,[1] D. Fernandez,[2] A. Fiasson,[33] G. Fontaine,[15] A. Förster,[3] M. Füßling,[11] M. Gajdus,[7] Y. A. Gallant,[2] T. Garrigoux,[19] H. Gast,[3] B. Giebels,[15] J. F. Glicenstein,[21] D. Göring,[8] M.-H. Grondin,[3,13] M. Grudzińska,[22] S. Häffner,[8] J. D. Hague,[3] J. Hahn,[3] J. Harris,[9] G. Heinzelmann,[1] G. Henri,[30] G. Hermann,[3] O. Hervet,[18] A. Hillert,[3] J. A. Hinton,[31] W. Hofmann,[3] P. Hofverberg,[3] M. Holler,[11] D. Horns,[1] A. Jacholkowska,[19] C. Jahn,[8] M. Jamrozy,[34] M. Janiak,[12] F. Jankowsky,[13] I. Jung,[8] M. A. Kastendieck,[1] K. Katarzyński,[35] U. Katz,[8] S. Kaufmann,[13] B. Khélifi,[15] M. Kieffer,[19] S. Klepser,[10] D. Klochkov,[20] W. Kluźniak,[12] T. Kneiske,[1] D. Kolitzus,[17] Nu. Komin,[33] K. Kosack,[21] S. Krakau,[16] F. Krayzel,[33] P. P. Krüger,[23,3] H. Laffon,[27,15] G. Lamanna,[33] J. Lefaucheur,[14] M. Lemoine-Goumard,[27] J.-P. Lenain,[19] D. Lennarz,[3] T. Lohse,[7] A. Lopatin,[8] C.-C. Lu,[3] V. Marandon,[3] A. Marcowith,[2] G. Maurin,[33] N. Maxted,[29] M. Mayer,[11] T. J. L. McComb,[9] M. C. Medina,[21] J. Méhault,[27†] U. Menzler,[16] M. Meyer,[1] R. Moderski,[12] M. Mohamed,[13] E. Moulin,[21] T. Murach,[7] C. L. Naumann,[19] M. de Naurois,[15] D. Nedbal,[36] J. Niemiec,[32] S. J. Nolan,[9] L. Oakes,[7] S. Ohm,[31,37] E. de Oña Wilhelmi,[3] B. Opitz,[1] M. Ostrowski,[34] I. Oya,[7] M. Panter,[3] R. D. Parsons,[3] M. Paz Arribas,[7] N. W. Pekeur,[23] G. Pelletier,[30] J. Perez,[17] P.-O. Petrucci,[30] B. Peyaud,[21] S. Pita,[14] H. Poon,[3] G. Pühlhofer,[20] M. Punch,[14] A. Quirrenbach,[13] S. Raab,[8] M. Raue,[1] A. Reimer,[17] O. Reimer,[17] M. Renaud,[2] R. de los Reyes,[3] F. Rieger,[3] L. Rob,[36] S. Rosier-Lees,[33] G. Rowell,[29] B. Rudak,[12] C. B. Rulten,[18] V. Sahakian,[6,5] D. A. Sanchez,[3⋆] A. Santangelo,[20] R. Schlickeiser,[16] F. Schüssler,[21] A. Schulz,[10] U. Schwanke,[7] S. Schwarzburg,[20] S. Schwemmer,[13] H. Sol,[18] G. Spengler,[7] F. Spieß,[1] Ł. Stawarz,[35] R. Steenkamp,[28] C. Stegmann,[11,10] F. Stinzing,[8]

⋆E-mail: biteau@in2p3.fr (JB); yvonne.becherini@lsw.uni-heidelberg.de (YB); david.sanchez@mpi-hd.mpg.de (DAS); jeremy.s.perkins@nasa.gov (JSP)
† Funded by contract ERC-StG-259391 from the European Community.

K. Stycz,[10] I. Sushch,[7,23] A. Szostek,[34] J.-P. Tavernet,[19] R. Terrier,[14] M. Tluczykont,[1] C. Trichard,[33] K. Valerius,[8] C. van Eldik,[8] G. Vasileiadis,[2] C. Venter,[23] A. Viana,[3] P. Vincent,[19] H. J. Völk,[3] F. Volpe,[3] M. Vorster,[23] S. J. Wagner,[13] P. Wagner,[7] M. Ward,[9] M. Weidinger,[16] R. White,[31] A. Wierzcholska,[34] P. Willmann,[8] A. Wörnlein,[8] D. Wouters,[21] M. Zacharias,[16] A. Zajczyk,[12,2] A. A. Zdziarski,[12] A. Zech,[18] H.-S. Zechlin,[1] J. S. Perkins,[38,39★] R. Ojha,[40,41] J. Stevens,[42] P. G. Edwards[43] and M. Kadler[44,38]

[1]*Institut für Experimentalphysik, Universität Hamburg, Luruper Chaussee 149, D-22761 Hamburg, Germany*
[2]*Laboratoire Univers et Particules de Montpellier, Université Montpellier 2, CNRS/IN2P3, CC 72, Place Eugène Bataillon, F-34095 Montpellier Cedex 5, France*
[3]*Max-Planck-Institut für Kernphysik, PO Box 103980, D-69029 Heidelberg, Germany*
[4]*Dublin Institute for Advanced Studies, 31 Fitzwilliam Place, Dublin 2, Ireland*
[5]*National Academy of Sciences of the Republic of Armenia, 375019 Yerevan, Armenia*
[6]*Yerevan Physics Institute, 2 Alikhanian Brothers St, 375036 Yerevan, Armenia*
[7]*Institut für Physik, Humboldt-Universität zu Berlin, Newtonstr. 15, D-12489 Berlin, Germany*
[8]*Physikalisches Institut, Universität Erlangen-Nürnberg, Erwin-Rommel-Str. 1, D-91058 Erlangen, Germany*
[9]*Department of Physics, University of Durham, South Road, Durham DH1 3LE, UK*
[10]*DESY, D-15735 Zeuthen, Germany*
[11]*Institut für Physik und Astronomie, Universität Potsdam, Karl-Liebknecht-Strasse 24/25, D-14476 Potsdam, Germany*
[12]*Nicolaus Copernicus Astronomical Center, ul. Bartycka 18, PL-00-716 Warsaw, Poland*
[13]*Landessternwarte, Universität Heidelberg, Königstuhl, D-69117 Heidelberg, Germany*
[14]*APC, AstroParticule et Cosmologie, Université Paris Diderot, CNRS/IN2P3, CEA/Irfu, Observatoire de Paris, Sorbonne Paris Cité, 10, rue Alice Domon et Léonie Duquet, F-75205 Paris Cedex 13, France*
[15]*Laboratoire Leprince-Ringuet, Ecole Polytechnique, CNRS/IN2P3, F-91128 Palaiseau, France*
[16]*Institut für Theoretische Physik, Lehrstuhl IV: Weltraum und Astrophysik, Ruhr-Universität Bochum, D-44780 Bochum, Germany*
[17]*Institut für Astro- und Teilchenphysik, Leopold-Franzens-Universität Innsbruck, A-6020 Innsbruck, Austria*
[18]*LUTH, Observatoire de Paris, CNRS, Université Paris Diderot, 5 Place Jules Janssen, F-92190 Meudon, France*
[19]*LPNHE, Université Pierre et Marie Curie Paris 6, Université Denis Diderot Paris 7, CNRS/IN2P3, 4 Place Jussieu, F-75252, Paris Cedex 5, France*
[20]*Institut für Astronomie und Astrophysik, Universität Tübingen, Sand 1, D-72076 Tübingen, Germany*
[21]*DSM/Irfu, CEA Saclay, F-91191 Gif-Sur-Yvette Cedex, France*
[22]*Astronomical Observatory, The University of Warsaw, Al. Ujazdowskie 4, PL-00-478 Warsaw, Poland*
[23]*Unit for Space Physics, North-West University, Potchefstroom 2520, South Africa*
[24]*Harvard-Smithsonian Center for Astrophysics, 60 garden Street, Cambridge, MA 02138, USA*
[25]*School of Physics, University of the Witwatersrand, 1 Jan Smuts Avenue, Braamfontein, Johannesburg, 2050 South Africa*
[26]*Oskar Klein Centre, Department of Physics, Stockholm University, Albanova University Center, SE-10691 Stockholm, Sweden*
[27]*Université Bordeaux 1, CNRS/IN2P3, Centre d'Études Nucléaires de Bordeaux Gradignan, F-33175 Gradignan, France*
[28]*Department of Physics, University of Namibia, Private Bag 13301, Windhoek, Namibia*
[29]*School of Chemistry and Physics, University of Adelaide, Adelaide 5005, Australia*
[30]*UJF-Grenoble 1/CNRS-INSU, Institut de Planétologie et d'Astrophysique de Grenoble (IPAG) UMR 5274, F-38041 Grenoble, France*
[31]*Department of Physics and Astronomy, The University of Leicester, University Road, Leicester LE1 7RH, UK*
[32]*Instytut Fizyki Jądrowej PAN, ul. Radzikowskiego 152, PL-31-342 Kraków, Poland*
[33]*Laboratoire d'Annecy-le-Vieux de Physique des Particules, Université de Savoie, CNRS/IN2P3, F-74941 Annecy-le-Vieux, France*
[34]*Obserwatorium Astronomiczne, Uniwersytet Jagielloński, ul. Orla 171, PL-30-244 Kraków, Poland*
[35]*Toruń Centre for Astronomy, Nicolaus Copernicus University, ul. Gagarina 11, PL-87-100 Toruń, Poland*
[36]*Faculty of Mathematics and Physics, Institute of Particle and Nuclear Physics, Charles University, V Holešovičkách 2, CZ-180 00 Prague 8, Czech Republic*
[37]*School of Physics and Astronomy, University of Leeds, Leeds LS2 9JT, UK*
[38]*CRESST and Astroparticle Physics Laboratory NASA/GSFC, Greenbelt, MD 20771, USA*
[39]*University of Maryland, Baltimore County, 1000 Hilltop Circle, Baltimore, MD 21250, USA*
[40]*Astrophysics Science Division, NASA Goddard Space Flight Center, Greenbelt, MD 20771, USA*
[41]*Institute for Astrophysics and Computational Sciences, Catholic University of America, USA*
[42]*CSIRO Astronomy and Space Science, Locked Bag 194, Narrabri, NSW 2390, Australia*
[43]*CSIRO Astronomy and Space Science, PO Box 76, Epping, NSW 1710, Australia*
[44]*Institut für Theoretische Physik und Astrophysik, Universität Würzburg, D-97074 Würzburg, Germany*

Accepted 2013 June 13. Received 2013 June 12; in original form 2013 May 21

ABSTRACT

A deep observation campaign carried out by the High Energy Stereoscopic System (HESS) on Centaurus A enabled the discovery of γ-rays from the blazar 1ES 1312−423, 2° away from

the radio galaxy. With a differential flux at 1 TeV of $\phi(1\,\mathrm{TeV}) = (1.9 \pm 0.6_{\mathrm{stat}} \pm 0.4_{\mathrm{sys}}) \times 10^{-13}\,\mathrm{cm^{-2}\,s^{-1}\,TeV^{-1}}$ corresponding to 0.5 per cent of the Crab nebula differential flux and a spectral index $\Gamma = 2.9 \pm 0.5_{\mathrm{stat}} \pm 0.2_{\mathrm{sys}}$, 1ES 1312−423 is one of the faintest sources ever detected in the very high energy ($E > 100\,\mathrm{GeV}$) extragalactic sky. A careful analysis using three and a half years of *Fermi* Large Area Telescope (*Fermi*-LAT) data allows the discovery at high energies (E > 100 MeV) of a hard spectrum ($\Gamma = 1.4 \pm 0.4_{\mathrm{stat}} \pm 0.2_{\mathrm{sys}}$) source coincident with 1ES 1312−423. Radio, optical, UV and X-ray observations complete the spectral energy distribution of this blazar, now covering 16 decades in energy. The emission is successfully fitted with a synchrotron self-Compton model for the non-thermal component, combined with a blackbody spectrum for the optical emission from the host galaxy.

Key words: radiation mechanisms: non-thermal – galaxies: active – BL Lacertae objects: individual: 1ES 1312–423 – galaxies: jets – gamma-rays: galaxies.

1 INTRODUCTION

BL Lac objects and flat spectrum radio quasars (FSRQs) are the two flavours of active galactic nuclei (AGN) which compose the blazar class. Characterized by a powerful jet aligned at small angles to the line of sight, these two types of blazars have distinct signatures in the optical band: FSRQs exhibit broad emission lines while BL Lac objects show featureless spectra (e.g. Stickel et al. 1991; Stocke et al. 1991; Laurent-Muehleisen et al. 1999). The typical spectral energy distribution (SED) of BL Lac objects exhibits two bumps, one at low energy, from radio to X-rays, and the other at higher energies, in the γ-ray energy band. If the first bump peaks below the infrared to UV domain, a BL Lac can be labelled as a low-frequency-peaked object while it is usually classified as a high-frequency-peaked object (HBL) if the emission is peaked in the UV/X-ray band (Padovani & Giommi 1995). Blazar emission models account for the low-energy component with synchrotron emission of relativistic electrons accelerated in the jet, while the origin of the high-energy (HE) bump remains under debate. Leptonic scenarios attribute it to inverse Compton scattering of the electrons off the self-generated synchrotron photon field (synchrotron self-Compton or SSC models, e.g. Band & Grindlay 1985), or off externally provided photons e.g. from broad-line regions, a dusty torus or the accretion disc (external Compton or EC models, e.g. Dermer & Schlickeiser 1993). The very high energy [VHE, ($E \gtrsim 100\,\mathrm{GeV}$)] γ-ray emission in hadronic scenarios can be explained by the interactions of relativistic protons with ambient photons (as, e.g. in Mannheim 1993) or magnetic fields (as, e.g. in Aharonian 2000).

Initially detected in X-rays by the *Einstein* observatory (Gioia et al. 1990), 1ES 1312−423 was subsequently extracted from optical sky surveys by Stocke et al. (1991), who classified it as a BL Lac object. Optical imaging by Falomo & Ulrich (2000) resolved a nucleus 10 times fainter than the host galaxy in the *R* band. The soft X-ray spectrum derived from *BeppoSAX* observations by Wolter et al. (1998) refined the classification of the AGN as an HBL. Based on its high ratio of X-ray to radio flux and through a simple modelling, Stecker, de Jager & Salamon (1996) proposed this low-redshift HBL ($z = 0.105 \pm 0.001$, Rector et al. 2000) as a potential VHE γ-ray emitter, though with a very faint predicted flux above 1 TeV of 0.7 per cent of the Crab nebula flux.[1]

[1] The Crab units used in this paper refer to the index Γ and differential flux ϕ_0 at 1 TeV derived by Aharonian et al. (2006) from Crab nebula observations, i.e. $\Gamma = 2.63$ and $\phi_0 = 3.45 \times 10^{-11}\,\mathrm{cm^{-2}\,s^{-1}\,TeV^{-1}}$.

This faint HBL is located at the coordinates $(\alpha_{J2000}, \delta_{J2000}) = (13^{\mathrm{h}}15^{\mathrm{m}}03\overset{\mathrm{s}}{.}4,\ -42^{\circ}36'50'')$ (Mao 2011) and it lies at the edge of the field of view (FoV) of the telescopes of the High Energy Stereoscopic System (HESS) for observations targeted 2° away, on the radio-galaxy Centaurus A. In the VHE domain, Centaurus A is a faint source (0.8 per cent of the Crab nebula flux) that was discovered after an extensive HESS observation campaign (Aharonian et al. 2009a), also unveiling an excess coincident with the position of 1ES 1312−423 (see Section 2.1).

The *Fermi* Large Area Telescope (*Fermi*-LAT) first and second catalogues, i.e. the 1LAC (Abdo et al. 2010d), 1FGL (Abdo et al. 2010a), 2LAC (Ackermann et al. 2011) and 2FGL (Nolan et al. 2012), do not include a counterpart of 1ES 1312−423 at HE (between 100 MeV and 100 GeV). However, motivated by the HESS detection at VHE, a careful modelling of the Centaurus A giant lobes emission by the *Fermi*-LAT collaboration, using 3.5 yr of data, reveals a faint HE source coincident with 1ES 1312−423 (see Section 2.2).

The HE and VHE spectra derived by the *Fermi*-LAT and HESS collaborations are combined with multiwavelength data from *Swift* X-Ray Telescope (XRT) and Ultraviolet/Optical Telescope (UVOT), Automatic Telescope for Optical Monitoring (ATOM) and Australia Telescope Compact Array (ATCA) (see Sections 2.3, 2.4, 2.5 and 2.6) with the purpose of understanding the properties of the source. A standard one-zone SSC model and a blackbody emission model for the host galaxy are used to describe the current and the archival data, detailed in Section 3.1. The modelling and its physical implications are discussed in Section 3.2.

2 OBSERVATIONS AND ANALYSIS

2.1 HESS data set and analysis

HESS is an array of four Cherenkov telescopes located 1800 m above sea level in the Khomas Highland, Namibia (23°16′18″S, 16°30′01″E). Each telescope covers a large FoV of 5° diameter and consists of a 13 m diameter optical reflector (Bernlöhr et al. 2003) and a camera composed of 960 photomultipliers (Vincent et al. 2003). The coincident detection of a Cherenkov flash from an extended air shower with at least two telescopes triggers the acquisition of its images and allows a good cosmic ray background rejection above ∼100 GeV (Funk et al. 2004).

Located 2° away from Centaurus A, 1ES 1312−423 benefits from the intensive observation campaign on this FoV. The data set studied in this paper is selected with standard quality criteria (stable detector and good weather, as described in Aharonian et al. 2006), which

yielded 150.6 h exposure time from 2004 April to 2010 July at an average zenith angle of 24°. The correction of this total exposure time for the decrease in efficiency due to the large offset (∼2°) of the source with respect to the camera centre leads to a total corrected exposure of 48.4 h. This decrease in efficiency does not bias the analysis of the data set, as shown in Appendix A.

Data are analysed using the analysis method described in Becherini et al. (2011) and cross-checked with the method of de Naurois & Rolland (2009). These methods both achieve enhanced background rejection and sensitivity at low energies with respect to standard analysis methods (e.g. Aharonian et al. 2006). The first procedure, used to derive the results shown in this paper, is based on a boosted decision tree technique, with a multivariate combination of discriminant parameters from the Hillas (see, e.g. Aharonian et al. 2006) and the 3D-model (Lemoine-Goumard, Degrange & Tluczykont 2006) analysis methods.

Both analysis methods are applied using a minimum image intensity of 60 photoelectrons (p.e.) yielding a threshold energy of 280 GeV, and give consistent results. The VHE significance map of 1ES 1312−423 showing the presence of the two AGN in the same FoV (see Fig. 1) is obtained with the *Ring* background modelling method (Berge, Funk & Hinton 2007) and with an inner ring radius of 0.°7. The smoothed, background-subtracted map of the number of γ-rays observed around the position of 1ES 1312−423, obtained with the same background modelling method, is shown in the right-hand panel of Fig. 1.

The distribution of the squared angular distance θ^2 between the reconstructed shower direction and the test position, obtained by projecting the two-dimensional maps on the radial direction, is shown in Fig. 2, for ON-source and normalized OFF-source events. The distribution of the excess, shown in an inset, is compatible with the HESS point spread function (PSF, black line in the inset on Fig. 2). The total excess, obtained with the *Reflected* background modelling method (Aharonian et al. 2006) within a radius of 0.°102 (PSF 68 per cent containment radius), corresponds to 149 ± 28 events[2] at the test position of the source, for an overall significance[3] of 5.7σ.

The fit of a point-like source model convolved with the HESS PSF to the excess events locates the emission at $(\alpha_{\rm J2000}, \delta_{\rm J2000}) = (13^{\rm h}14^{\rm m}58.^{\rm s}5 \pm 4.2^{s}_{\rm stat} \pm 1.3^{s}_{\rm sys},\ -42°35'49'' \pm 48''_{\rm stat} \pm 20''_{\rm sys})$, which is compatible with the test position at the 1σ level.

The differential energy spectrum $\phi(E) = {\rm d}N/{\rm d}E$ of the VHE γ-ray emission is derived above 280 GeV with a forward folding technique (Piron et al. 2001). A fit with a power law (PWL) $\phi(E) = \phi(E_0) \times (E/E_0)^{-\Gamma}$ yields best-fitting parameters $\Gamma = 2.85 \pm 0.47_{\rm stat} \pm 0.20_{\rm sys}$ and $\phi(E_0) = (1.18 \pm 0.35_{\rm stat} \pm 0.24_{\rm sys}) \times 10^{-13}\,{\rm cm^{-2}\,s^{-1}\,TeV^{-1}}$ at the decorrelation energy $E_0 = 1.18$ TeV. This corresponds to a differential flux at 1 TeV of $\phi(1{\rm TeV}) = (1.89 \pm 0.58_{\rm stat} \pm 0.39_{\rm sys}) \times 10^{-13}\,{\rm cm^{-2}\,s^{-1}\,TeV^{-1}}$, equivalent to 0.5 per cent of the Crab nebula differential flux. 1ES 1312−423 is thus one of the faintest extragalactic sources ever detected in the VHE band.

The 1σ confidence contour of the PWL fit, referred to as the 'butterfly', together with the spectral points and residuals, are shown in Fig. 3. The numbers of excess events $N_{i,\rm det}$ detected in the five energy bins i do not significantly differ from the numbers of expected events $N_{i,\rm th}$, yielding $X^2 = \sum_i (N_{i,\rm det} - N_{i,\rm th})^2/\sigma^2_{N_{i,\rm det}}$ of 1.03 with 3 degrees of freedom.

The VHE light curve, computed on a year-by-year time-scale, is shown in the top panel of Fig. 4. Since the number of excess events is statistically low, a smaller temporal binning does not provide more information on variability. A search for flux variability is carried out using the fractional variance $F_{\rm var}$ (see, e.g. Vaughan et al. 2003), an estimator of the intrinsic variance normalized to the square of the mean flux, which is computed by quadratically subtracting the contribution of the experimental uncertainties from the observed variance.

The measured normalized excess variance of $F^2_{\rm var} = 0.17 \pm 0.44$ is compatible with zero, indicating that any potential variability is washed out by measurement uncertainties. A 99 per cent confidence level (CL) upper limit, calculated using the method of Feldman & Cousins (1998) under the hypothesis of a Gaussian uncertainty, is $F^2_{\rm var} \leq 1.30$, which corresponds to $F_{\rm var}({\rm year}) \lesssim 1.1$. This limit means that the VHE γ-ray flux of 1ES 1312−423 did not vary on average by more than a factor of 1.1 on the time-scale of one year.

2.2 *Fermi*-LAT data set and analysis

The LAT on board the *Fermi* satellite is a pair-conversion telescope designed to detect γ-rays from 20 MeV up to energies greater than 300 GeV. The characteristics and performance of the instrument are described in Atwood et al. (2009). The LAT observes the full sky every 3 h (two orbits) and each source is in the FoV for ∼30 min during this period.

The LAT data on 1ES 1312−423 analysed hereafter span 3.5 yr, from 2008 August 4 (MJD 54682) to 2012 February 16 (MJD 55973). Only events with a high probability of being photons (belonging to the SOURCE class), with zenith angles less than 100° and with reconstructed energies between 300 MeV and 300 GeV are retained. The `P7SOURCE_V6` Instrumental Response Functions (IRFs) are used to describe the detector and the data are analysed with the SCIENCETOOLS v9r23p1.

A binned likelihood analysis chain (Mattox et al. 1996; Abdo et al. 2009), implemented in the GTLIKE tool, is used to best match the spectral model with the front and back events,[4] which are analysed separately to maximize the sensitivity.

The analysis is carried out on a region of interest of 15° around the 1ES 1312−423 coordinates, where the events are grouped in 0.°1 × 0.°1 bins and using 10 energy bins per decade between 300 MeV and 300 GeV. The sky model is constructed using the standard model for Galactic interstellar diffuse emission, an isotropic background component [5] and the sources of the 2FGL catalogue (Nolan et al. 2012), with the spectral models derived therein. The parameters of the sources close to 1ES 1312−423 (≤3°) are left free during the fitting procedure, while the parameters of more distant sources are frozen to their 2FGL values. The extended γ-ray emission from the Centaurus A lobes is modelled using a spatial template based

[2] The total numbers of ON- and OFF-source events are $N_{\rm ON} = 780$ and $N_{\rm OFF} = 30120$, respectively, with a background-normalization factor $\alpha \simeq 0.0209$.

[3] Since 1ES 1312−423, whose location is precisely measured, is a known candidate γ-ray emitter (Stecker et al. 1996), no trial factor is accounted for in the significance.

[4] See section 2.2.1 of Atwood et al. (2009) for definition of front and back events.

[5] The backgrounds are described in the files `gal_2yearp7v6_v0.fits` and `iso_p7v6source.txt` available from the FSSC http://fermi.gsfc.nasa.gov/ssc/.

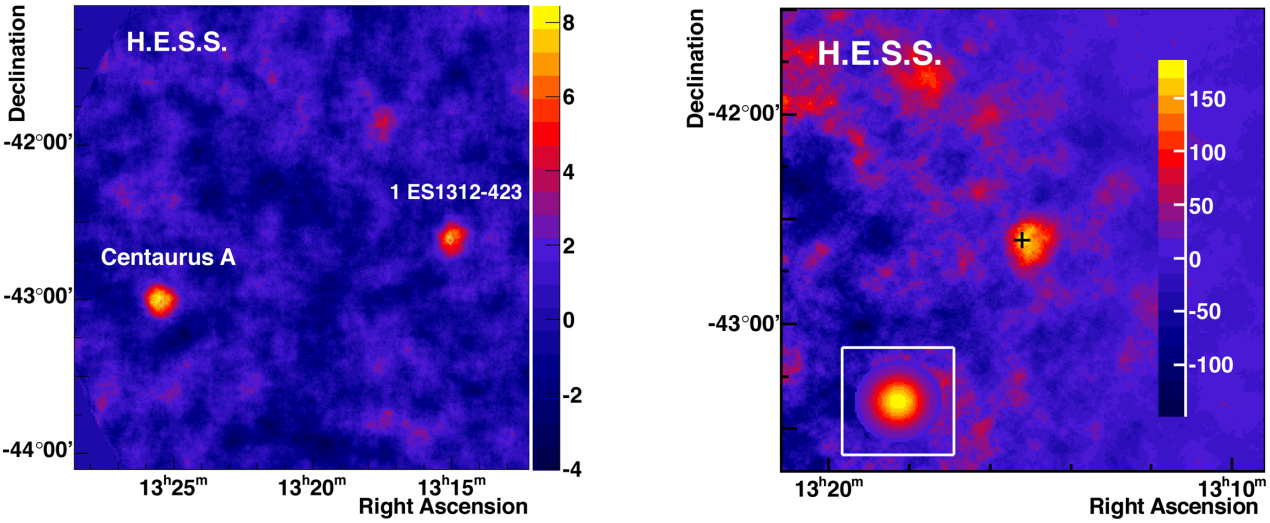

Figure 1. Left: significance map of the VHE γ-ray emission of the radio galaxy Centaurus A and of the BL Lac 1ES 1312−423 in right ascension and declination (J2000). Right: map of the excess γ-rays measured with HESS, smoothed with the PSF (68 per cent containment radius of 0.°10 for these analysis cuts). The cross represents the test position of the source. The bottom-left inset shows the expected γ-ray excess distribution from a point-like source.

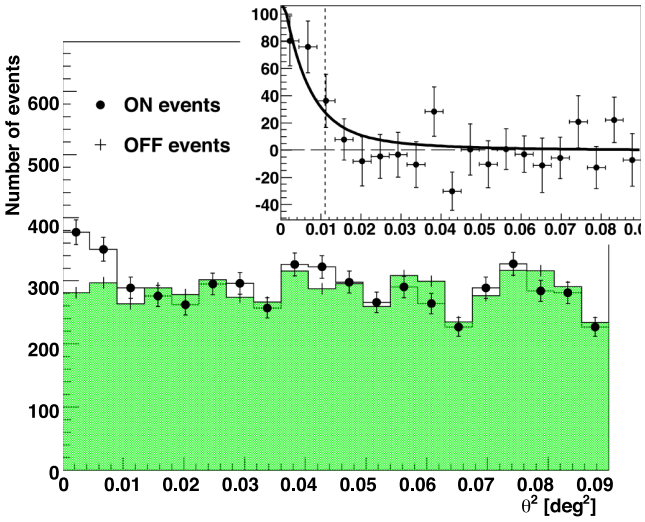

Figure 2. The distribution of the squared angular distance between the test position and the reconstructed shower direction for ON-source events (black points) and normalized OFF-source events (green shaded area). In the inset, background-subtracted distribution of the squared angular distance in deg^2 between the fitted position and the reconstructed shower direction, representing the excess events from this source. The superimposed line is a fit of the PSF to the data. The PSF 68 per cent containment radius of 0.°102 is shown as a vertical dashed line.

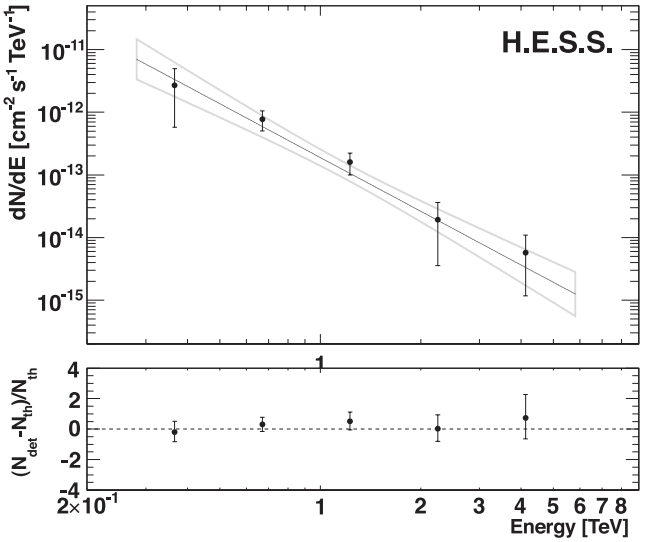

Figure 3. HESS differential energy spectrum of 1ES 1312−423. The grey butterfly represents the 1σ contour of the best PWL model that fits the data in the observed energy range (280 GeV–5.8 TeV). The lower panel shows the fit residuals, i.e. $(N_{\rm det} - N_{\rm th})/N_{\rm th}$, where $N_{\rm det}$ and $N_{\rm th}$ are the detected and expected number of excess events, respectively.

on the 22 GHz *Wilkinson Microwave Anisotropy Probe* image of the region (Hinshaw et al. 2009), as in Abdo et al. (2010b). The validity of the model is checked by subtracting the predicted count map from the observed one, yielding no significant residuals. A point-like source is added to the sky model at the test position of 1ES 1312−423, whose spectrum is described with a PWL. The positions of the sources are frozen to the input values during the minimization process.

With a test statistic of the likelihood analysis of 32.6, approximately 5.7σ, 1ES 1312−423 is detected by the LAT with a flux of $(1.59 \pm 0.48_{\rm stat}\,^{+0.14}_{-0.54\ \rm sys}) \times 10^{-15}$ photons cm^{-2} s^{-1} MeV^{-1} at the decorrelation energy $E_0 = 22.5$ GeV and a photon index $\Gamma = 1.44 \pm 0.42_{\rm stat}\,^{+0.20}_{-0.25\ \rm sys}$, where the systematic uncertainties are evaluated using the bracketing IRFs method (Ackermann et al. 2012). The low average flux measured with *Fermi*-LAT using 3.5 yr of data is consistent with the non-detection (TS < 25) of 1ES 1312−423 in the second catalogue (interpolated TS of ∼19 assuming a steady-state emission). The upper end of the energy range covered by *Fermi*-LAT is set to 300 GeV since the three highest photon energies measured in a 95 per cent containment radius are 102, 181 and 294 GeV. Four flux points are computed in energy bins of equal width in log scale by performing a GTLIKE analysis with the photon index of the source frozen to its best-fitting value. The same analysis is performed to compute the light curve on time intervals of six months, shown in the middle panel of Fig. 4. Upper limits at the 95 per cent CL are computed for spectral and temporal bins with TS < 4. The variability indicator

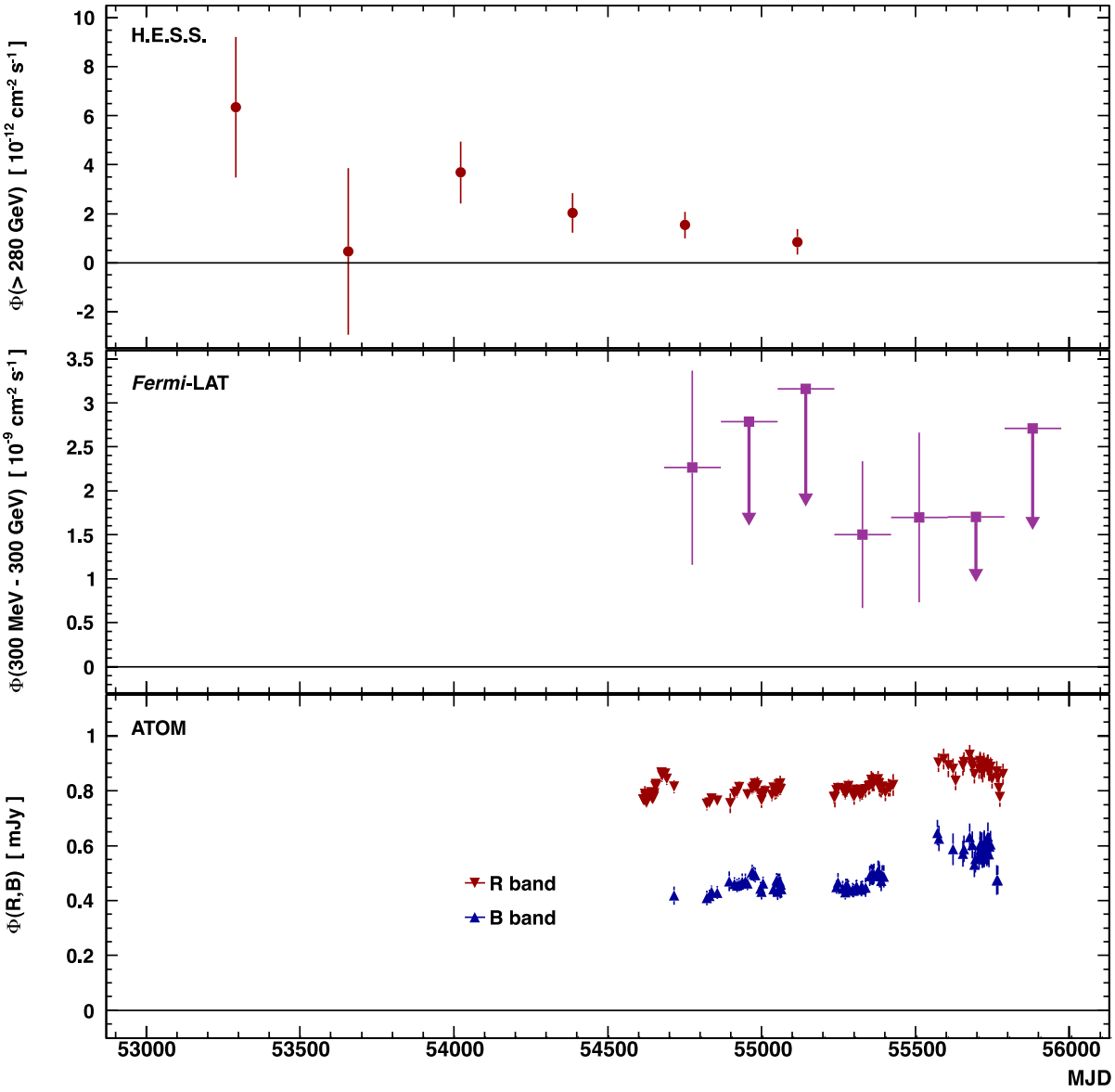

Figure 4. Top: integral VHE γ-ray flux of 1ES 1312−423 above the threshold energy measured with HESS Middle: integral HE γ-ray flux of 1ES 1312−423 in the *Fermi*-LAT energy band. 95 per cent CL upper limits are computed for the time bins with TS < 4. Bottom: dereddened flux measured by ATOM in the *R* and *B* bands, represented with downward and upward pointing triangles, respectively.

provided by the likelihood ratio method in Nolan et al. (2012) is computed as $TS_{var} = 13.1$ for six degrees of freedom, showing no significant variations with an equivalent chance probability of 41 per cent.

2.3 *Swift*/XRT data set and analysis

The HESS collaboration triggered an observation of 1ES 1312−423 with the space-based *Swift* X-ray observatory (Burrows et al. 2005), performed on 2011 January 25 at 01:22 UTC (ObsID 00031915001) with 4.7 ks exposure time. The photon-counting mode data are processed with the standard XRTPIPELINE tool (HEASOFT 6.12), with the source and background-extraction regions defined as a 20-pixel (∼4.7 arcsec) radius circle, the latter being centred nearby the former without overlapping. The source region count rate is ∼0.7 counts s^{-1}, a rate considered to be at the limit of risk of pile up, but a King function fit to the PSF shows no evidence for pile up in the inner part of the source region. Also, the results of the spectral analysis are compatible within errors to those found with a source region defined by an annulus of 20-pixel outer radius and 4-pixel (∼0.9 arcsec) inner radius, thus excluding 58 per cent of the events.

The XRTMKARF tool is used to generate a dedicated Ancillary Response Function (ARF) at the location of the source in the FoV, along with the latest spectral redistribution matrices from the calibration database (CALDB). The *Swift*/XRT spectrum is re-binned to have at least 20 counts per bin using `grppha`, yielding a usable energy range between 0.3 and 7.0 keV. Multiple model spectra are tested with PYXSPEC v.1.0.1, the response functions `swxpc0to12s6_20010101v013` and the dedicated ARF. Systematic errors on the *Swift*/XRT spectra and absolute flux are less than 3 and 10 per cent, respectively (Godet et al. 2009).

The XRT spectrum is first studied using the weighted average column density of Galactic H I $N_H = 7.8 \times 10^{20}$ cm^{-2} that is

Table 1. Fit parameters and uncertainties for the spectral models and column density values studied in Section 2.3. The parameters described in columns 4 and 5 depend on the model (power law, log parabola and broken power law) as discussed in the text. The χ^2, numbers of degrees of freedom and corresponding probabilities are shown in columns 7 and 8. The last column indicates the significance of the fit improvement for models nested with the PWL model with fixed column density.

Model	$N_{\rm H} \times 10^{20}$ ($\rm cm^{-2}$)	ϕ_0 ($10^{-3}\rm cm^{-2}\,s^{-1}\,keV^{-1}$)	Γ or a or Γ_0	b or Γ_1	$E_{\rm break}$ (keV)	χ^2/ndf	P_{χ^2}	LRT(H_0 = PWL)
PWL	7.8	5.7 ± 0.1	1.91 ± 0.02	–	–	155.0/122	23 per cent	–
BPWL	7.8	5.9 ± 0.1	1.67 ± 0.07	2.18 ± 0.08	1.6 ± 0.2	124.8/120	36 per cent	5.1σ
LP	7.8	6.1 ± 0.1	$1.73^{+0.04}_{-0.05}$	0.47 ± 0.09	–	122.4/121	45 per cent	5.7σ
LP – min $N_{\rm H}$	6.7	5.9 ± 0.1	1.66 ± 0.04	0.55 ± 0.09	–	122.4/121	45 per cent	–
LP – max $N_{\rm H}$	9.1	6.3 ± 0.1	1.81 ± 0.04	0.38 ± 0.09	–	122.6/121	44 per cent	–
LP – free $N_{\rm H}$	7.3 ± 3.6	6.0 ± 0.7	1.70 ± 0.23	0.51 ± 0.27	–	122.3/120	42 per cent	5.4σ
PWL – free $N_{\rm H}$	14.2 ± 1.3	7.3 ± 0.4	2.14 ± 0.05	–	–	125.8/121	37 per cent	5.4σ

extracted from the Leiden/Argentine/Bonn (LAB) survey (Kalberla et al. 2005) with the $N_{\rm H}$ tool from HEASARC.[6] The best-fitting PWL model $\phi(E) = \phi_0(E/E_0)^{-\Gamma}$, PWL in Table 1, yields a reduced χ^2 of 1.1, with deviations from zero in the residuals at both low and high energies. A likelihood ratio test (LRT) prefers the simplest smoothly curved function, a log parabola (LP) $\phi(E) = \phi_0(E/E_0)^{-a-b\log(E/E_0)}$, at the 5.7σ level with a reduced χ^2 of 1.01. The best-fitting curvature parameter b measured in the spectrum of 1ES 1312−423 is a characteristic of the TeV candidates observed in X-rays as noted by Massaro et al. (2008, 2011a). A broken power law (BPWL), $\phi(E) = \phi_0(E/E_0)^{-\Gamma_0\times\Theta(E<E_{\rm break})-\Gamma_1\times\Theta(E>E_{\rm break})}$, where Θ is the Heaviside function, is also an acceptable model with a reduced χ^2 of 1.04, and a break of $\Delta\Gamma = \Gamma_1 - \Gamma_0 \simeq 0.51 \pm 0.11$ consistent with those usually found in X-ray-selected BL Lac-type objects (Sambruna, Maraschi & Urry 1996; Urry et al. 1996; Wolter et al. 1998). The LP has one parameter fewer than the BPWL and is therefore used in the following.

In addition to the uncertainties on the optical depth correction for the spin temperature of the gas (see, e.g. the discussion in Johannesson et al. 2010), the values of $N_{\rm H}$ from the LAB survey show significant variations within one degree of the source, ranging from a minimal value of $N_{\rm H} = 6.7 \times 10^{20}\,\rm cm^{-2}$ to a maximal value of $N_{\rm H} = 9.1 \times 10^{20}\,\rm cm^{-2}$. This could indicate that fluctuations of the interstellar medium on scales smaller than the LAB survey's half-power beam-width of $\simeq 0.^\circ 6$ exist but are barely detectable. Checking for fluctuations on smaller scales in the *IRAS* 100 μm [7] dust maps, which have a better resolution and correlate extremely well at high Galactic latitudes with maps of H I emission (Schlegel, Finkbeiner & Davis 1998), no evidence for large fluctuations in a 5 arcmin radius centred on 1ES 1312−423 is found. Following the relation of Güver & Özel (2009), the estimated total extinction in the V band of $\rm A(V) = 0.336 \pm 0.016$ mag corresponds to $N_{\rm H} = \rm A(V) \times (2.21 \pm 0.09) \times 10^{21}\ cm^{-2} = (7.4 \pm 0.5) \times 10^{20}\ cm^{-2}$. The minimal and maximal $N_{\rm H}$ values of the LAB survey are compatible with $\pm 3\sigma$ deviations from this value, and are hence used as conservative limits on the column density in the following. This slightly changes the best-fitting parameters of the log-parabolic spectrum (fourth and fifth line in Table 1), the low-energy slope a being most affected by these variations, as shown in Fig. 5.

For reference, leaving the column density as a free parameter with the log-parabolic model yields a flat X-ray spectrum in νF_ν up to ∼1 keV, marginally preferred to a PWL model with free column density (an LRT yielding a 1.9σ improvement). The latter would suggest additional absorbing material with a column density $\geq 7 \times 10^{20}\ \rm cm^{-2}$, for which little or no evidence has been found so far in BL Lac objects (Perlman et al. 2005). The curvature, which is compatible with values usually found for X-ray bright BL Lac objects, appears to be intrinsic to the source and the first bump in the SED of 1ES 1312−423 should then peak in the energy band covered by *Swift*/XRT.

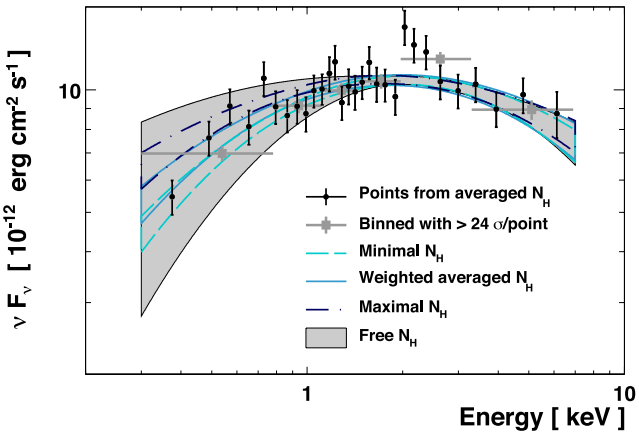

Figure 5. *Swift*/XRT spectrum of 1ES 1312−423. The column density of hydrogen $N_{\rm H}$ varies greatly over the $1^\circ \times 1^\circ$ FoV, three values of $N_{\rm H}$ (dashed line for minimal, solid line for weighted average and dotted/dashed line for maximal) are used to de-absorb the spectrum. The grey butterfly represents the best LP model that fits the data in the observed energy range (0.3–7.0 keV) for a free column density.

2.4 *Swift*/UVOT analysis

Simultaneously with *Swift*/XRT observations, the *Swift*/UVOT (Roming et al. 2005) took six snapshots of 1ES 1312−423 with the filter $uvm2$ (224.6 nm). They are integrated with the UVOTIMSUM tool of the package HEASOFT 6.12 and analysed using the UVOTSOURCE tool, with circular ON and OFF regions of radius 5 arcsec. The background is estimated from different OFF regions, at least 25 arcsec away from the source. A change of the background regions impacts the reconstructed flux at the percent level. The magnitudes are dereddened according to the extinction laws of Draine (2003) with a total absorption at 224.6 nm $\rm A_\lambda = 1.1$ mag corresponding to the *IRAS* extinction mentioned in Section 2.3. The flux densities are computed from the magnitude according to the zero-points of Poole et al. (2008). The source does not show any sign of variability on the hour time-scale ($F^2_{\rm var}$(hour) < 0.012 at the 99 per cent

[6] http://heasarc.gsfc.nasa.gov/cgi-bin/Tools/w3nh/w3nh.pl
[7] Using the tool http://irsa.ipac.caltech.edu/applications/DUST/

confidence level), with an average flux at 224.6 nm of $(3.19 \pm 0.08) \times 10^{-12}$ erg cm^{-2} s^{-1}. Following Tramacere et al. (2007), a conservative systematic uncertainty on the UV flux of 15 per cent is adopted.

A joint fit of the UVOT measurement with the X-ray spectrum, adding the interstellar extinction directly to the model with the redden component set to the *IRAS* value, does not significantly change the results from Section 2.3, nor the estimate of the *Swift*/UVOT flux.

2.5 ATOM data set and analysis

Optical observations were performed with the ATOM telescope (Hauser et al. 2004) at the HESS site from 2008 May to 2011 August. Absolute flux values are calculated using differential photometry with 4 arcsec radius aperture for all filter bands, against four stars calibrated with photometric standards.

The 83 and 122 measurement points in the B and R bands, respectively, show small flux variations during the two years of observation, with fractional variances of 10.6 ± 0.9 and 4.0 ± 0.4 per cent, respectively. The observed average magnitudes $m_B = 17.87 \pm 0.02_{\rm stat} \pm 0.04_{\rm sys}$ and $m_R = 16.66 \pm 0.01_{\rm stat} \pm 0.02_{\rm sys}$ are converted to fluxes using absorptions of $A_\lambda(B) = 0.499$ and $A_\lambda(R) = 0.299$ mag (Draine 2003) and standard zero-points (Bessell 1990), yielding a total flux from the host and the nucleus of $\phi(B) = (3.33 \pm 0.05_{\rm stat} \pm 0.10_{\rm sys}) \times 10^{-12}$ and $\phi(R) = (3.47 \pm 0.02_{\rm stat} \pm 0.06_{\rm sys}) \times 10^{-12}$ erg cm^{-2} s^{-1}, the systematic uncertainty arising from flat-fielding as well as dark and bias corrections. The ATOM light curves in the B and R bands are shown in the bottom panel of Fig. 4.

2.6 ATCA observations

Radio observations of 1ES 1312−423 were made by the ATCA (Wilson et al. 2011) on 2012 May 10, using the array configuration EW352. Flux densities are calibrated against PKS 1934–638, the ATCA primary flux density calibrator. These observations were made with 2 GHz bandwidths provided by the Compact Array Broadband Backend (Wilson et al. 2011), centred on 5.5, 9.0, 17, 19, 38 and 40 GHz. At the lower four frequency bands, the source has a flux density of 9 mJy. It has a flux density of 6.5 mJy at 38 GHz and 4.6 mJy at 40 GHz. Thus, this source has a relatively flat radio spectrum with a spectral index of 0.20 ± 0.05. Uncertainties at the 3σ level on the flux density are conservatively estimated at 2 mJy.

The pointing model was updated for the 17/19 GHz and 38/40 GHz band observations by a five point cross scan on a nearby bright AGN. Scans at each frequency were 2 min in length and the source was at elevation 48° at 5/9 GHz and a few degrees higher at the highest frequencies, thus minimizing atmospheric effects. Data reduction followed standard procedures as described in Stevens et al. (2012). There are no signs of the source being extended on the $L = 4.4$ km maximum baselines in this array, for which the angular resolution goes down to 0.4 arcsec at 40 GHz.

3 MODELLING OF THE SPECTRAL ENERGY DISTRIBUTION

3.1 Comparison of archival and current data

The 1σ *Fermi*-LAT butterfly (300 MeV $< E <$ 300 GeV) and the HESS spectrum are represented by the empty and filled dark butterflies in Fig. 6. The HESS butterfly includes the systematic uncertainties on the index (∼0.20) and on the flux (∼20 per cent), added quadratically at the decorrelation energy to the statistical one. The systematic uncertainties on the *Fermi*-LAT spectral parameters are propagated in the same way. The *Fermi*-LAT spectral extension to VHE (dashed line), which is absorbed by the extragalactic background light (EBL) according to Franceschini, Rodighiero & Vaccari (2008), overshoots the HESS 1σ confidence contour. The difference between the spectral indexes is explained by intrinsic curvature, supported by the empirical relation of Abdo et al. (2010e) between the peak frequency $\nu^{\rm IC}_{\rm peak}$ of the HE bump and the HE photon index Γ, which reads $\log \nu^{\rm IC}_{\rm peak}[{\rm Hz}] = -4\Gamma + 31.6 = 26.2 \pm 1.4$, corresponding to a peak energy between ∼25 GeV and ∼15 TeV. The low statistics of the *Fermi*-LAT data at high energies (three photons above 100 GeV) does not enable a straightforward characterization of this peak energy. The *Fermi*-LAT and HESS fluxes differ by a factor of $r \sim 6$ at 300 GeV, with $\log_{10} r = 0.8 \pm 0.6_{\rm stat} \pm 0.3_{\rm sys}$, but the large statistical and systematic uncertainties do not suggest a significant discrepancy. Though no flux variations can be detected within the uncertainties, a more significant mismatch could be explained by the non-simultaneous sky coverage of HESS and *Fermi*-LAT, as shown in Fig 4. Since little variability in the spectral index is found at HE, irrespective of the blazar class (Abdo et al. 2010c), the emission model mostly aims at reproducing the slope observed at HE, and the VHE spectrum is used as a baseline for the normalization.

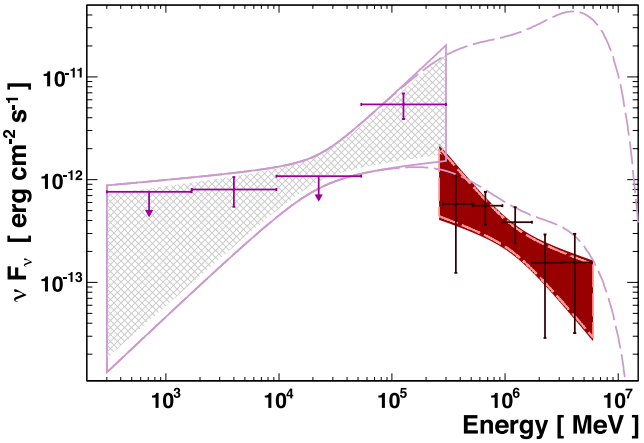

Figure 6. *Fermi*-LAT and HESS spectra, represented by the empty magenta and filled dark red butterflies, respectively. The HESS (resp. *Fermi*-LAT) spectrum includes statistical and systematic errors on the flux and index, for reference the 1σ statistical butterfly is shown in dashed light red (resp. hatched light magenta). The *Fermi*-LAT butterfly is extrapolated to VHE (dashed magenta), taking into account the EBL absorption according to Franceschini et al. (2008).

The SED of 1ES 1312−423 shown in Fig. 7 is derived from a compilation of the data analysed in this paper and of archival data. ATCA, ATOM and *Swift*/UVOT measurements are described in the top-right legend in Fig. 7. A conservative approach motivated the use of the *Swift*/XRT spectra corresponding to the minimal and maximal column densities (see Section 2.3). The uncertainty on the column density is thus practically treated as a systematic effect.

The archival data on 1ES 1312−423, which are detailed in the top-left legend in Fig. 7, are retrieved from online data bases.[8]

[8] http://vizier.u-strasbg.fr/viz-bin/VizieR, http://tools.asdc.asi.it/SED

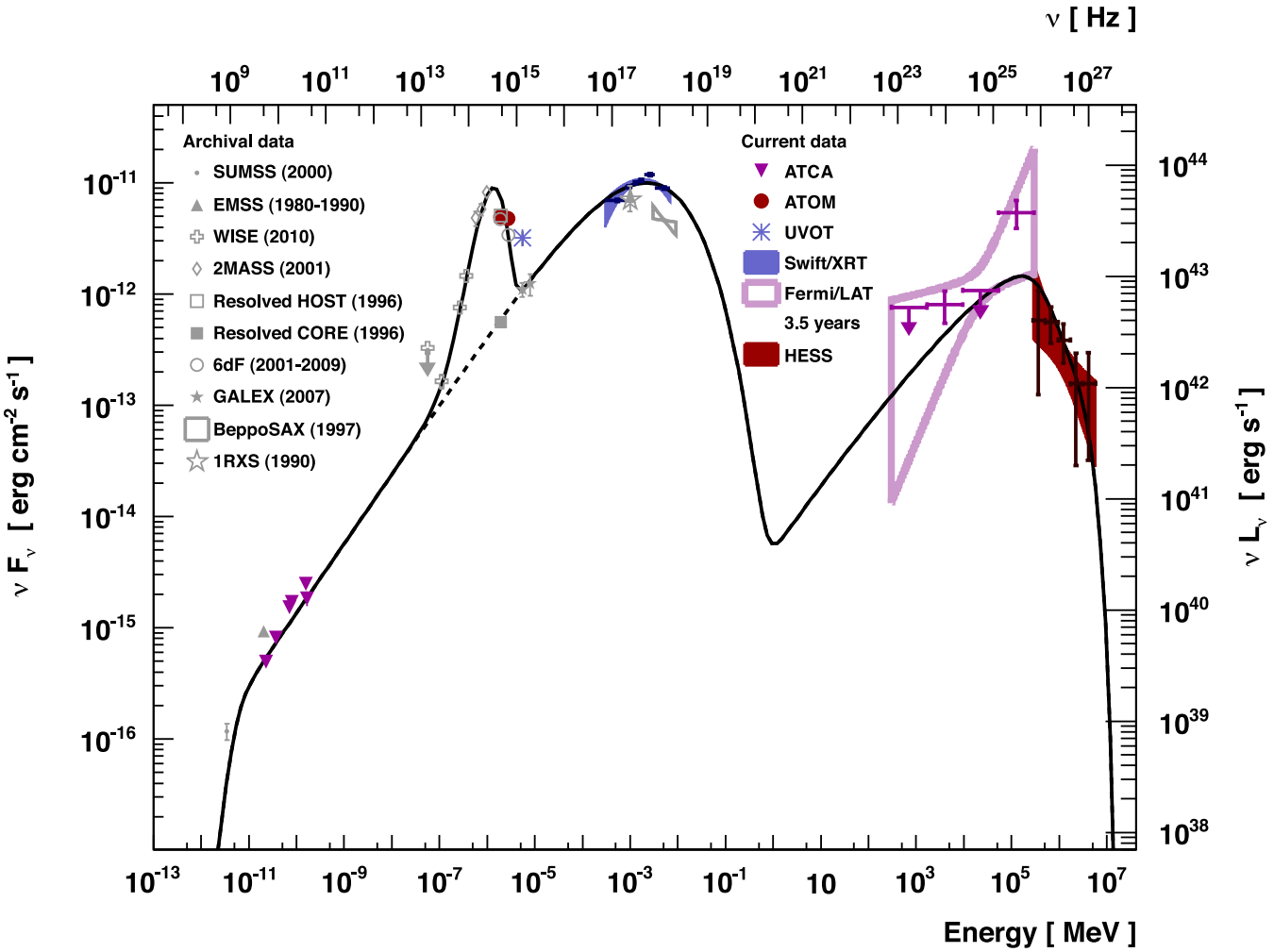

Figure 7. Spectral energy distribution of 1ES 1312−423. The archival data from radio to X-rays are detailed in the top-left legend, the period of observation being indicated between parentheses. The observations described in this paper consist of ATOM measurements in the *B* and *R* bands (full circles), *Swift*/UVOT measurement at 192.8 nm (asterisk symbol) and ATCA measurements at 5.5, 9.0, 17, 19, 38 and 40 GHz (filled downward-pointing triangles). *Swift*/XRT, HESS and *Fermi*-LAT spectra are represented by the butterflies (filled for the first two, empty for the last one). The data are modelled assuming a blackbody emission in the infrared–optical band while the radio and optical emission of the core as well as the X-ray, HE and VHE spectra are described with a one zone homogeneous SSC emission.

Infrared to UV data, which are dereddened consistently with Sections 2.32.4 and 2.5, are extracted from the *Wide-field Infrared survey* (*WISE*, Wright et al. 2010), from the 2MASS All-Sky Catalogue of Point Sources (Cutri et al. 2003), from the 6dF galaxy survey (Jones et al. 2009) and from the ultraviolet survey performed with Galaxy Evolution Explorer (GALEX; Martin et al. 2005). The UV fluxes measured with *GALEX* and with UVOT differ by a factor of 3. Both measurements are dereddened and the discrepancy can hardly be explained by the known uncertainties. A high-amplitude variability could explain the difference, though it is barely observed in the other energy bands on the time-scale of years. These two points are subsequently not included in the modelling, but are discussed *a posteriori* in Section 3.2. The optical data from the USNO-A2.0 (Monet 1998), the USNO-B1.0 (Monet et al. 2003) and the Guide Star (GSC2.3, Spagna et al. 2006) catalogues are not included because of flags indicating a probable association with a nearby star. X-ray and radio archival data are extracted from the Einstein Extended Medium Sensitivity Survey (EMSS; Gioia et al. 1990; Stocke et al. 1991), the *ROSAT* All-Sky Bright Source Catalogue (1RXS, Voges et al. 1999), the Spectral catlogue of *BeppoSAX* blazars (Donato, Sambruna & Gliozzi 2005) and the Sydney University Molonglo Sky Survey (SUMSS V2.1, Mauch et al. 2003).

Falomo & Ulrich (2000) imaged the source in the *R* band and derived an extension of the host galaxy equivalent to ∼2 arcsec within the standard Λ cold dark matter (ΛCDM) cosmological model ($\Omega_{\rm M} = 0.27$, $\Omega_\Lambda = 0.73$, $h_0 = 0.71$). The emission of the host galaxy, represented by an open square in Fig. 7, is 10 times brighter than the emission of the core represented by the filled square. The fluxes measured by ATOM and from the 6dF galaxy survey are corrected for the limited aperture, yielding 30 and 20 per cent greater flux values, respectively. The host galaxy is modelled with a blackbody emission, this thermal origin being supported by the absence of polarization and microvariability (Andruchow, Romero & Cellone 2005). This emission is constrained by the measurements from *WISE*, which do not probe synchrotron emission as occurs in brighter TeV BL Lac objects (Massaro et al. 2011b). The small amplitude of the variations detected in the ATOM band is fully consistent with the modelling, where the core emission represents *a posteriori* 10 per cent (resp. 20 per cent) of the total

emission in the R (resp. B) band.[9] Though not strictly contemporaneous, the radio, X-ray HE and VHE data, as well as the emission of the core resolved by Falomo & Ulrich (2000), are modelled assuming a non-thermal emission within a standard leptonic SSC scenario.

3.2 Modelling

A canonical, one zone, homogeneous, time-independent SSC model is used to interpret the multi wavelength data. A blob of plasma, filled with a constant tangled magnetic field B, is modelled by a spherical region of size R, and is assumed to move with a bulk Doppler factor δ (as, e.g. in Band & Grindlay 1985; Katarzyński, Sol & Kus 2001). The particle energy distribution (PED) of the electrons is described, as in Giebels, Dubus & Khélifi (2007), by a PWL of index p with an exponential cut-off $n(\gamma) = n_0 \gamma^{-p} \exp(-\gamma/\gamma_{\rm cut})$, where $\gamma = E/m_e c^2$ is the Lorentz factor of the electrons. The normalization factor of the PED n_0 is linked to the kinetic energy density of the electrons in the blob frame according to the equation $u_{e^-} = m_e c^2 \int_1^{+\infty} (\gamma - 1)\, n(\gamma)\, {\rm d}\gamma$. This variable yields better physical insights into the plasma properties than the normalization factor n_0, since it can be directly compared to the magnetic energy density in the blob frame $u_B = B^2/8\pi$.

The optical emission is modelled with a blackbody spectrum, as in Katarzyński, Sol & Kus (2003). The synchrotron self-absorption and the internal γ–γ absorption are taken into account according to Gould (1979) and the approximation of Coppi & Blandford (1990), respectively. The interaction of γ-rays with the EBL is modelled according to Franceschini et al. (2008). Finally, the luminosity distance of this source, located at a redshift $z = 0.105$ (Rector et al. 2000), is computed within the standard ΛCDM cosmological model, yielding a luminosity distance $D_L = 479$ Mpc.

Although SSC models are the simplest ones used to explain emission from BL Lac objects, they are usually underconstrained. The SSC model described herein has six parameters, three related to the PED (n_0, $\gamma_{\rm cut}$, p) and three related to the emission zone (R, B and δ). The index of the PED is constrained by the HE index and by the fluxes measured from radio wavelengths to X-rays, including the optical flux of the core measured by Falomo & Ulrich (2000). For a fixed index, the amplitude and location of the synchrotron peak are proportional to $n_0 \delta^4 R^3 B^2$ and $B \delta \gamma_{\rm cut}^2$, respectively (e.g. Band & Grindlay 1985), and can be fixed using the *Swift*/XRT spectrum. The very low energy part of the spectrum (radio data) is controlled by synchrotron self-absorption. This imposes a rather weak constraint since the radio flux, which could arise from larger scale structures, is only an upper limit on the emission of the blob. Three parameters can hence be tuned to fit the amplitude and location of the inverse Compton peak. Thus, whatever the freedom left by the uncertainty on HE and VHE γ-ray spectra, the model is degenerate.

To reduce this degeneracy, the inverse Compton bump is reproduced by constraining the magnetic field, the distance to equipartition ($|u_{e^-}/u_B - 1|$) and the Doppler factor. A short distance to equipartition ensures a small energy budget (e.g. Burbidge 1959). A small Doppler factor is motivated by the Lorentz factors ($\Gamma \sim 3$–4) inferred from the subluminal motion generally observed in TeV blazars or from the distribution of beamed objects within the BL Lac / radio galaxy unification scheme (cf. bulk Lorentz factor crisis, Henri & Saugé 2006).

[9] Knowing the fraction of the emission coming from the core, a consistent fractional variance of the core flux of ∼50 per cent is derived in both R and B ATOM bands.

Table 2. Parameters of the one zone SSC model shown in Fig. 7.

Index p	$\gamma_{\rm min}$	$\gamma_{\rm cut}$	B (mG)	δ	u_{e^-}/u_B	R ($\times 10^{17}$ cm)
1.75	1	1.0×10^6	10	7	45	2.4

In addition to the SSC model parameters, the infrared to optical data impose the amplitude and temperature of the blackbody emission, which do not increase the degeneracy of the model. The model of the archival and current data is represented in Fig. 7. The parameters of the SSC model are detailed in Table 2. The blackbody emission peaks at a temperature $T = 4500$ K for a total luminosity $\mathcal{L}_{BB} = 3.1 \times 10^{44}$ erg s^{-1}. The host galaxy UV emission should be much lower than the flux measured with *Swift*/UVOT, which is hence expected to be of non-thermal origin, but is not matched by our minimal SSC model. This could be taken into account at the expense of adding parameters to the PED or adding extra components (e.g. as in Sol, Pelletier & Asseo 1989). The bolometric luminosity of the emitting region is $\mathcal{L} = 1.8 \times 10^{45}$ erg s^{-1}, ranging from 1 to 10 per cent of the Eddington luminosity for fiducial values of the black hole mass between 10^9 and 10^8 solar masses.

The parameters of the PED fitting the data are not far from those derived by Giebels et al. (2007) for Markarian 421, with electron energies between $\gamma_{\rm min} \sim 1$ and $\gamma_{\rm cut} \sim 10^6$ and a rather hard index $p = 1.75$, smaller than the canonical value of 2 derived in diffusive shock acceleration. The size of the emitting region $R \sim 80$ mpc and the amplitude of the magnetic field $B = 10$ mG are similar to those derived for PKS 2155–304 by Aharonian et al. (2009b). A lower limit on the variability time-scale of the order of a week can be derived from the size of the emitting region and the Doppler factor $\delta = 7$. This value of the Doppler factor sets a limit on the Lorentz factor of the emitting region $\Gamma \geq \delta/2 = 3.5$. The VHE data cannot be reproduced with a system in equipartition and require a ratio as large as $u_{e^-}/u_B = 45$. Such deviations from equipartition in favour of the particles are not unusual when modelling HBLs (see, e.g. Mankuzhiyil et al. 2012, for Mrk 421 and Mrk 501). A break in the index of $\Delta p = 1$ is expected at the electron energy for which the cooling time (here given by the synchrotron loss rate) equals the time needed to escape the region, typically R/c to $R/(c/3)$ (cf. e.g. Tavecchio, Maraschi & Ghisellini 1998). This reads $t_{\rm cool} = [\frac{4}{3} \frac{\sigma_T c}{m_e c^2} \gamma_{\rm break}\, u_B]^{-1} \sim R/c$ and for the parameters considered herein the break energy is of the order of the cut-off in the PED, thus not affecting the self-consistency of the modelling.

4 CONCLUSION

The HESS collaboration reports the discovery of the blazar 1ES 1312−423 in the VHE γ-ray domain. In spite of being one of the faintest VHE γ-ray sources ever detected, with a differential flux at 1 TeV equivalent to 0.5 per cent of the Crab nebula differential flux, the long observation campaign on its neighbour Centaurus A unveiled VHE γ-ray emission from 1ES 1312−423 at the $\sim 6\sigma$ level. The analysis of 3.5 years of data from *Fermi*-LAT brought to light an HE spectrum that is one of the hardest derived for a blazar by the *Fermi*-LAT Collaboration, though with a large uncertainty on the index. The combination of these HE and VHE spectra together with ATCA, ATOM and *Swift* measurements allows for the

first time the broad-band SED of this HBL-type blazar to be investigated. A blackbody emission models the flux of the host galaxy and a simple SSC scenario reproduces the non-thermal emission in the radio, X-ray, HE and VHE bands.

After 3.5 years of observations with *Fermi*-LAT and intensive campaigns with HESS, the extragalactic sky begins to reveal sources as faint as few thousandths of the Crab nebula flux. The long-term sky monitoring with *Fermi*-LAT combined with the next-generation Cherenkov observatory, the Cherenkov Telescope Array (CTA; Actis et al. 2011), will be the important ingredients to reveal a broad picture of blazars' HE and VHE behaviour.

ACKNOWLEDGEMENTS

The support of the Namibian authorities and of the University of Namibia in facilitating the construction and operation of HESS is gratefully acknowledged, as is the support by the German Ministry for Education and Research (BMBF), the Max Planck Society, the French Ministry for Research, the CNRS-IN2P3 and the Astroparticle Interdisciplinary Programme of the CNRS, the UK Particle Physics and Astronomy Research Council (PPARC), the IPNP of the Charles University, the South African Department of Science and Technology and National Research Foundation, and by the University of Namibia. We appreciate the excellent work of the technical support staff in Berlin, Durham, Hamburg, Heidelberg, Palaiseau, Paris, Saclay, and in Namibia in the construction and operation of the equipment.

The *Fermi* LAT Collaboration acknowledges generous ongoing support from a number of agencies and institutes that have supported both the development and the operation of the LAT as well as scientific data analysis. These include the National Aeronautics and Space Administration and the Department of Energy in the United States, the Commissariat à l'Energie Atomique and the Centre National de la Recherche Scientifique/Institut National de Physique Nucléaire et de Physique des Particules in France, the Agenzia Spaziale Italiana and the Istituto Nazionale di Fisica Nucleare in Italy, the Ministry of Education, Culture, Sports, Science and Technology (MEXT), High Energy Accelerator Research Organization (KEK) and Japan Aerospace Exploration Agency (JAXA) in Japan, and the K. A. Wallenberg Foundation, the Swedish Research Council and the Swedish National Space Board in Sweden.

Additional support for science analysis during the operations phase is gratefully acknowledged from the Istituto Nazionale di Astrofisica in Italy and the Centre National d'Études Spatiales in France.

The ATCA is part of the Australia Telescope National Facility which is funded by the Commonwealth of Australia for operation as a National Facility managed by CSIRO. This research was funded in part by NASA through *Fermi* Guest Investigator grant NNH09ZDA001N (proposal number 31263). This research was supported by an appointment to the NASA post-doctoral Programme at the Goddard Space Flight Center, administered by Oak Ridge Associated Universities through a contract with NASA.

This research has made use of the NASA/IPAC Extragalactic Database (NED) which is operated by the Jet Propulsion Laboratory, California Institute of Technology, under contract with the National Aeronautics and Space Administration.

This research has made use of the VizieR catalogue access tool, CDS, Strasbourg, France.

We are grateful to Kim Page for her help on UVOT analysis issues.

REFERENCES

Abdo A. A. et al., 2009, Astrophys. J. Suppl., 183, 46
Abdo A. A. et al., 2010a, ApJS, 188, 405
Abdo A. A. et al., 2010b, Sci, 328, 725
Abdo A. A. et al., 2010c, ApJ, 710, 1271
Abdo A. A. et al., 2010d, ApJ, 715, 429
Abdo A. A. et al., 2010e, ApJ, 716, 30
Ackermann M. et al., 2011, ApJ, 743, 171
Ackermann M. et al., 2012, ApJS, 203, 4
Actis M. et al., 2011, Exp. Astron., 32, 193
Aharonian F. A., 2000, New Astron., 5, 377
Aharonian F. et al. (H. E. S. S. Collaboration), 2006, A&A, 457, 899
Aharonian F. et al. (H. E. S. S. Collaboration), 2009a, ApJ, 695, L40
Aharonian F. et al. (H. E. S. S. Collaboration), 2009b, ApJ, 696, L150
Andruchow I., Romero G. E., Cellone S. A., 2005, A&A, 442, 97
Atwood W. B. et al., 2009, ApJ, 697, 1071
Band D. L., Grindlay J. E., 1985, ApJ, 298, 128
Becherini Y., Djannati-Ataï A., Marandon V., Punch M., Pita S., 2011, Astropart. Phys., 34, 858
Berge D., Funk S., Hinton J., 2007, A&A, 466, 1219
Bernlöhr K. et al., 2003, Astropart. Phys., 20, 111
Bessell M. S., 1990, PASP, 102, 1181
Burbidge G. R., 1959, ApJ, 129, 849
Burrows D. N. et al., 2005, Space Sci. Rev., 120, 165
Coppi P. S., Blandford R. D., 1990, MNRAS, 245, 453
Cutri R. M. et al., 2003, VizieR Online Data Catalog, 2246, 0
de Naurois M., Rolland L., 2009, Astropart. Phys., 32, 231
Dermer C. D., Schlickeiser R., 1993, ApJ, 416, 458
Donato D., Sambruna R. M., Gliozzi M., 2005, A&A, 433, 1163
Draine B. T., 2003, ARA&A, 41, 241
Falomo R., Ulrich M.-H., 2000, A&A, 357, 91
Feldman G. J., Cousins R. D., 1998, Phys. Rev. D, 57, 3873
Franceschini A., Rodighiero G., Vaccari M., 2008, A&A, 487, 837
Funk S. et al., 2004, Astropart. Phys., 22, 285
Giebels B., Dubus G., Khélifi B., 2007, A&A, 462, 29
Gioia I. M., Maccacaro T., Schild R. E., Wolter A., Stocke J. T., Morris S. L., Henry J. P., 1990, ApJS, 72, 567
Godet O. et al., 2009, A&A, 494, 775
Gould R. J., 1979, A&A, 76, 306
Güver T., Özel F., 2009, MNRAS, 400, 2050
Hauser M., Möllenhoff C., Pühlhofer G., Wagner S. J., Hagen H.-J., Knoll M., 2004, Astron. Nachr., 325, 659
Henri G., Saugé L., 2006, ApJ, 640, 185
Hinshaw G. et al., 2009, ApJS, 180, 225
Johannesson G., Moskalenko I., Digel S., 2010, preprint (arXiv:1002.0081)
Jones D. H. et al., 2009, MNRAS, 399, 683
Kalberla P. M. W., Burton W. B., Hartmann D., Arnal E. M., Bajaja E., Morras R., Poeppel W. G. L., 2005, VizieR Online Data Catalog, 8076, 0
Katarzyński K., Sol H., Kus A., 2001, A&A, 367, 809
Katarzyński K., Sol H., Kus A., 2003, A&A, 410, 101
Laurent-Muehleisen S. A., Kollgaard R. I., Feigelson E. D., Brinkmann W., Siebert J., 1999, ApJ, 525, 127
Lemoine-Goumard M., Degrange B., Tluczykont M., 2006, Astropart. Phys., 25, 195
Mankuzhiyil N., Ansoldi S., Persic M., Rivers E., Rothschild R., Tavecchio F., 2012, ApJ, 753, 154
Mannheim K., 1993, A&A, 269, 67
Mao L. S., 2011, New Astron., 16, 503
Martin D. C. et al., 2005, ApJ, 619, L1
Massaro F., Tramacere A., Cavaliere A., Perri M., Giommi P., 2008, A&A, 478, 395
Massaro F., Paggi A., Elvis M., Cavaliere A., 2011a, ApJ, 739, 73
Massaro F., D'Abrusco R., Ajello M., Grindlay J. E., Smith H. A., 2011b, ApJ, 740, L48
Mattox J. R. et al., 1996, ApJ, 461, 396
Mauch T., Murphy T., Buttery H. J., 2003, MNRAS, 342, 1117

Monet D. G., 1998, Am. Astron. Soc., Vol. 30, The 526,280,881 Objects In The USNO-A2.0 Catalog. BAAS, p. 1427
Monet D. G. et al., 2003, AJ, 125, 984
Nolan P. L. et al., 2012, ApJS, 199, 31
Padovani P., Giommi P., 1995, ApJ, 444, 567
Perlman E. S. et al., 2005, ApJ, 625, 727
Piron F. et al., 2001, A&A, 374, 895
Poole T. S. et al., 2008, MNRAS, 383, 627
Rector T. A., Stocke J. T., Perlman E. S., Morris S. L., Gioia I. M., 2000, AJ, 120, 1626
Roming P. W. A. et al., 2005, Space Sci. Rev., 120, 95
Sambruna R. M., Maraschi L., Urry C. M., 1996, ApJ, 463, 444
Schlegel D. J., Finkbeiner D. P., Davis M., 1998, ApJ, 500, 525
Sol H., Pelletier G., Asseo E., 1989, MNRAS, 237, 411
Spagna A. et al., 2006, Mem. Soc. Astron. Ital., 77, 1166
Stecker F. W., de Jager O. C., Salamon M. H., 1996, ApJ, 473, L75
Stevens J. et al., 2012, in Ojha R., Thompson D. J., Dermer C., eds, Proc. Fermi and Jansky, Our Evolving Understanding of AGN, St Michaels, MD. preprint (arXiv:1205.2403)
Stickel M., Padovani P., Urry C. M., Fried J. W., Kuehr H., 1991, ApJ, 374, 431
Stocke J. T., Morris S. L., Gioia I. M., Maccacaro T., Schild R., Wolter A., Fleming T. A., Henry J. P., 1991, ApJS, 76, 813
Tavecchio F., Maraschi L., Ghisellini G., 1998, ApJ, 509, 608
Tramacere A. et al., 2007, A&A, 467, 501
Urry C. M., Sambruna R. M., Worrall D. M., Kollgaard R. I., Feigelson E. D., Perlman E. S., Stocke J. T., 1996, ApJ, 463, 424
Vaughan S., Edelson R., Warwick R. S., Uttley P., 2003, MNRAS, 345, 1271
Vincent P. et al., 2003, in Kajita T., Asaoka Y., Kawachi A., Matsubara Y., Sasaki M., eds, Proc. Conf. Int. Cosm. Ray, Vol. 5, Performance of the HESS Cameras. p. 2887
Voges W. et al., 1999, A&A, 349, 389
Wilson W. E. et al., 2011, MNRAS, 416, 832
Wolter A. et al., 1998, A&A, 335, 899
Wright E. L. et al., 2010, AJ, 140, 1868

APPENDIX A: PERFORMANCE OF HESS ANALYSIS FOR A SOURCE AT LARGE OFFSET AND IN AN ACCEPTANCE GRADIENT

In this appendix, we investigate the reliability of the VHE γ-ray spectrum of 1ES 1312−423 as derived from observations taken at large offset angle. HESS observations are mostly performed in *wobble* mode, i.e. pointed along a circle of radius $\sim 0.^\circ 5$ centred on the target. This value is an optimum between a decrease of the radial acceptance for an increasing offset and an increase of the number of regions used for background estimation. The large number of observations all around the source provides a locally flat acceptance field. Centaurus A being the target of the observations studied in this paper, 1ES 1312−423 is located in a strong gradient of acceptance as shown in Fig. A1.

HESS systematically took data at several offsets from the position of the Crab nebula, the brightest and most studied source in the HESS sky (Aharonian et al. 2006), in order to determine the γ-ray acceptance in the FoV. To check the reliability of the analysis at large offsets, observations with similarly large offsets from the Crab nebula are selected to reproduce the observational conditions of 1ES 1312−423. The selected data set corresponds thus to an average offset from the nominal position of $\sim 1.^\circ 9$ ($\sim 2^\circ$ for 1ES 1312−423) and a strong gradient of acceptance at the source location, as shown in Fig. A2.

These data are analysed using the method described in Becherini et al. (2011). The minimum image intensity of 60 p.e. yields an energy threshold of 680 GeV for a mean zenith angle of 50°. Because of the relatively low statistics on the data set, a PWL model is preferred to fit the spectrum.[10] The parameters of the fit are compared in Fig. A3 to those published in Aharonian et al. (2006), where the 1σ, 2σ and 3σ confidence contours are plotted in the differential-flux-at-1 TeV over PWL-index plane. The PWL spectrum obtained with the selected runs is compatible at the 1σ level with the published spectrum, confirming the reliability of the spectral analysis of the data acquired by HESS on 1ES 1312−423.

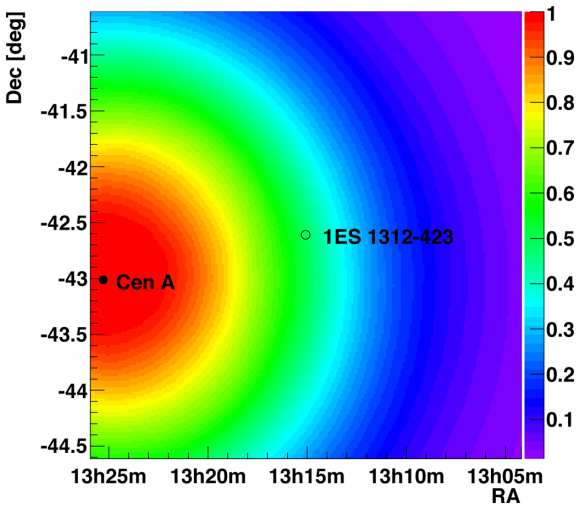

Figure A1. Normalized acceptance map of the HESS FoV around 1ES 1312−423. The map is computed using the measured hadronic events, assumed uniform in the FoV. The maximum value, normalized to 1, corresponds to the location of Centaurus A, target of the runs studied in this paper. 1ES 1312−423 is located in a strong gradient of exposure approximately 2° from the target of observations.

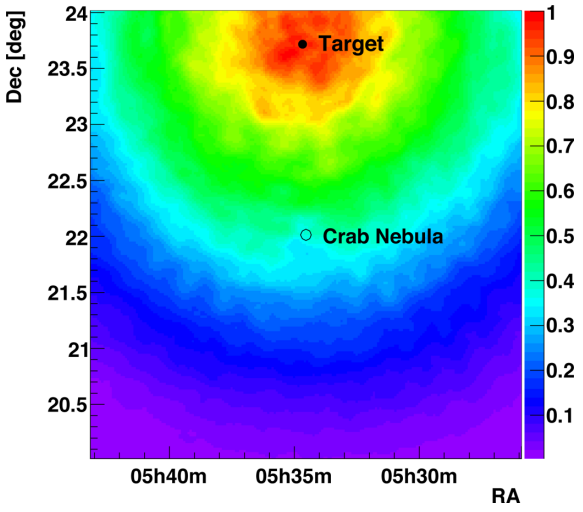

Figure A2. Normalized acceptance map of HESS FoV for selected runs on the Crab nebula. The runs are chosen to reproduce the observational conditions of 1ES 1312−423, locating the Crab nebula in a strong gradient of exposure, approximately $1.^\circ 9$ from the hypothetical target.

[10] Note that an exponential cut-off PWL model is a better representation for larger data sets, such as studied in Aharonian et al. (2006).

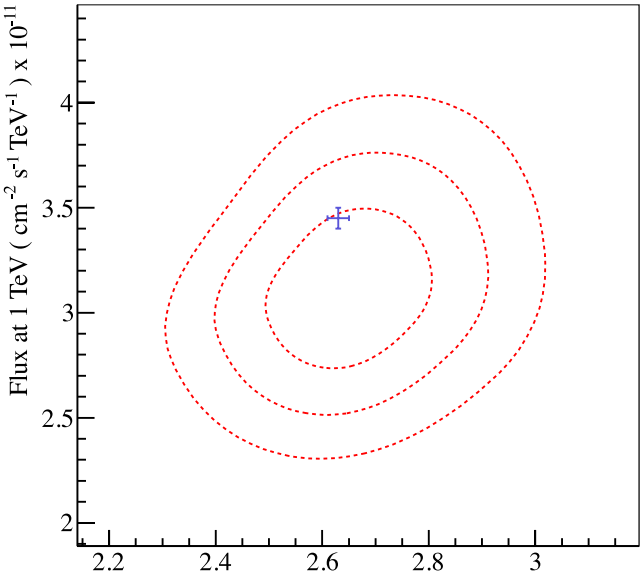

Figure A3. Confidence contours (1σ, 2σ and 3σ levels) of the spectral parameters matching the data from the Crab nebula. The spectrum is fitted with a PWL model, characterized by the differential flux at 1 TeV and the PWL index Γ. The best-fitting parameters are compatible with the spectrum derived with a larger data set in Aharonian et al. (2006), represented by the blue cross.

This paper has been typeset from a TEX/LATEX file prepared by the author.